Structural and thermal modeling of a *z*-axis rate integrating gyroscope

2003 J. Micromech. Microeng. 13 229

(http://iopscience.iop.org/0960-1317/13/2/310)

INSTITUTE OF PHYSICS PUBLISHING JOURNAL OF MICROMECHANICS AND MICROENGINEERING

J. Micromech. Microeng. **13** (2003) 229–237 PII: S0960-1317(03)54963-4

Structural and thermal modeling of a *z*-axis rate integrating gyroscope

C C Painter and A M Shkel

Microsystems Laboratory, Department of Mechanical and Aerospace Engineering, University of California, Irvine, CA 92697, USA

E-mail: cpainter@uci.edu and ashkel@uci.edu

Received 21 October 2002, in final form 10 December 2002
Published 13 January 2003
Online at stacks.iop.org/JMM/13/229

Abstract

This paper presents results of structural and thermal modeling of a *z*-axis rate integrating gyroscope. A strain energy method is used to obtain a structural model of the device, which is verified using finite element analysis. Based on a parametric analysis, an appropriate micromachining technology suitable for the fabrication of the gyroscope is identified. A sensitivity study shows that the operational modes of the proposed gyroscope remain matched under thermal and stress fluctuations, whereas a device with a commonly used H-type suspension shows a 31% frequency mismatch under thermal loading of 23.67 °C or 9 MPa of compressive stress.

(Some figures in this article are in colour only in the electronic version)

1. Introduction

The necessity for low cost and high performance inertial sensors has been the force driving development of microelectromechanical (MEM) gyroscopes. By virtue of sizes and fabrication costs magnitudes lower than their macro-world counterparts, micromachined gyroscopes offer a wide range of applications [1], ranging from satellite attitude sensing to rollover detection in automobiles. By combining multiple gyroscopes and accelerometers on a single chip, complete with on-board integrated electronics, full position and rate sensing can be achieved. Currently, there is an ongoing effort to design gyroscopes with increasingly improved sensitivity, bandwidth and resistivity to errors.

Most micromachined gyroscopes sense angular rates using vibrational elements. A structure is driven into resonance and rotation induced Coriolis force causes the transfer of energy from the drive vibrational mode to a sense vibrational mode. The magnitude of energy transferred is proportional to the rate of rotation. Inherent in all micromachined gyroscopes are sensing errors that manifest themselves in the form of angle random walk and bias drift [1]. In applications where it is necessary to integrate the rate signal to obtain the position, these errors are also integrated, thus magnifying the error. In these cases, it is more advantageous to measure the angle directly in order to avoid the effect of error integration.

In contrast to a rate gyroscope, which sustains resonance along a drive axis, an ideal micromachined gyroscope working in full angle measurement mode consists of a structure in free vibration. Input rotation induced Coriolis force causes the line of oscillation to precess. This principle is best illustrated by the Foucault pendulum, whose precessing plane of oscillation is often used to illustrate the effect of Earth's rotation [2]. Although existing devices utilizing vibrational shell designs [3, 4] can potentially be used for full angle sensing, these designs have limited sense capacitance due to the restriction that all electrodes must be incorporated around the perimeter of the shell.

The device studied in this paper [5] utilizes a vibrational 'lumped mass system' with parallel plate electrostatic combs used for drive and sense (figure 1(*a*)). This comb configuration allows electrostatic forces to be applied along four different axes. Two of these axes, designated as the drive axes, are designed to apply control forces used for driving, frequency tuning and energy loss compensation. The other two axes, designated as the sense axes, are used to detect the displacement and velocity of the proof mass. The use of sense combs interwoven between the comb fingers of the proof mass increases the sense capacitance, and therefore the sense capabilities, of the device.

The device operates by first driving the proof mass into forced oscillation. Upon reaching the desired amplitude,

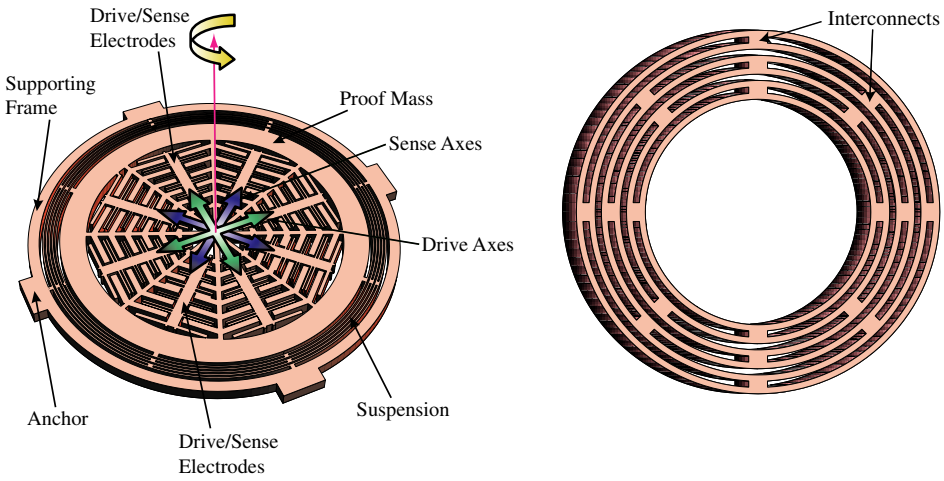

Figure 1. (*a*) The studied rate integrating gyroscope uses parallel plate combs for drive and sense. The drive combs are used to apply control forces to maintain oscillation of the proof mass while the sense combs are used to detect displacement and velocity. Rotation induced Coriolis force causes the line of oscillation to precess. The precession angle is equal to the angular displacement of the device [5]. (*b*) A proposed suspension design, consisting of a multiplicity of interconnected rings rigidly attached to an anchored frame, provides necessary isotropy required for the operation of this device.

the drive force is removed and the energy of the system is maintained using a specially designed control architecture [5, 6]. The rotation induced Coriolis force causes the line of oscillation to precess, which can be calculated from the detected position and velocity of the proof mass. This precession angle is equal to the angular displacement of the device.

In order for the line of oscillation to precess undisturbed, the gyroscope suspension must be isotropic to allow the principal axes of elasticity to be arbitrarily located in the plane of oscillation. Operation of the device with a non-isotropic suspension results in quadrature error manifested as an elliptical oscillation pattern that develops as the line of oscillation precesses away from the principal axes of elasticity [7]. This results in degraded performance of the gyroscope. A novel concentric ring suspension consisting of a multiplicity of concentric rings rigidly attached to an anchored frame is utilized to satisfy this condition (figure 1(*b*)).

The principles of operation of the rate integrating gyroscope are presented in section 2, followed by structural analysis of the device in section 3. The structural analysis utilizes a strain energy method to find a closed form expression for the in-plane stiffness of the suspension along the principal axes of elasticity, which is verified using finite element analysis. In addition, a parametric analysis of the suspension demonstrates the necessity for thick structural layers in order to prevent excitation of undesirable modes of operation. A comparative temperature sensitivity study between the ring suspension and an H-type spring suspension, a suspension type commonly used in MEMS applications [8], is presented in section 4. The effect of residual stress on the two suspensions is discussed. Residual stress is modeled by thermal loading of the suspensions and, based on the temperature sensitivity study, the effect of the resulting thermal stress is found.

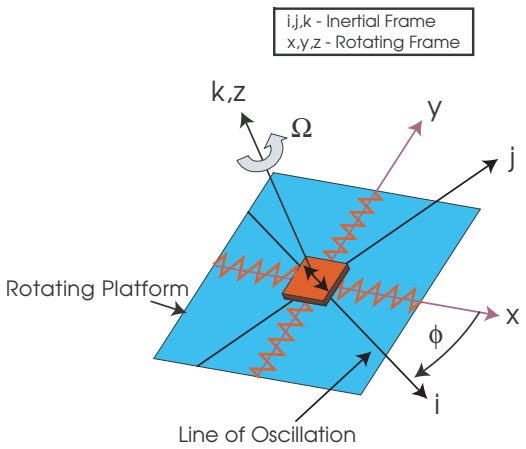

Figure 2. Mass-spring model of the z-axis angular gyroscope. $\{i, j, k\}$ is the inertial coordinate system and $\{x, y, z\}$ is the coordinate system attached to the rotating platform. In the absence of rotation, the inertial and rotating frames coincide. In the presence of rotation, the line of oscillation would be observed to precess by an angle ϕ with respect to the rotating coordinate system (or fixed with respect to the inertial frame).

2. Gyroscope principles

The gyroscope operates in the first two fundamental in-plane linear modes, therefore, the device is mathematically modeled as a lumped mass-spring system (figure 2). The model utilizes two coordinate systems: $\{i, j, k\}$—inertial coordinate system and $\{x, y, z\}$—coordinate system attached to the rotating platform. If the natural frequency of the system is large compared to the input rotation, and the stiffness in the z-direction is much larger than that in the other two orthogonal directions, then the out-of-plane dynamics can be ignored and the governing equations of motion are given by [6]

$$\ddot{x} + \omega_n^2 x - 2\Omega\dot{y} = 0, \qquad \ddot{y} + \omega_n^2 y + 2\Omega\dot{x} = 0. \tag{1}$$

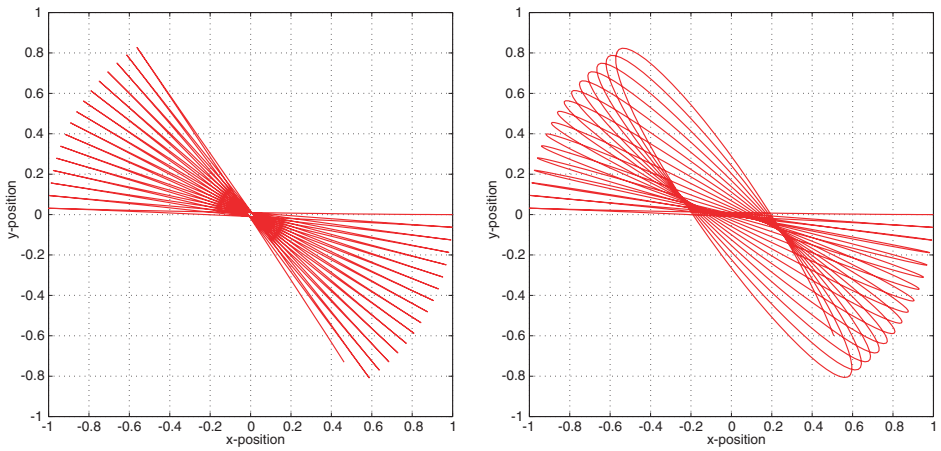

(*a*) (*b*)

Figure 3. (*a*) An isotropic suspension allows for the ideal operation of the gyroscope where the line of oscillation precesses undisturbed. (*b*) A non-isotropic suspension results in quadrature error manifested as an increasing elliptical oscillation pattern during precession.

If we assume an even mass distribution, then equation (1) can be written in a matrix form as

$$\begin{bmatrix} m & 0 \\ 0 & m \end{bmatrix} \begin{Bmatrix} \ddot{x} \\ \ddot{y} \end{Bmatrix} + \begin{bmatrix} k_{xx} & k_{xy} \\ k_{yx} & k_{yy} \end{bmatrix} \begin{Bmatrix} x \\ y \end{Bmatrix} + \begin{bmatrix} 0 & -2\Omega \\ 2\Omega & 0 \end{bmatrix} \begin{Bmatrix} \dot{x} \\ \dot{y} \end{Bmatrix} = \begin{Bmatrix} 0 \\ 0 \end{Bmatrix} \tag{2}$$

where m is the mass and if we assume an isotropic suspension, $k_{xx} = k_{yy}$ and $k_{xy} = k_{yx} = 0$. Since the stiffness is the same in the x- and y-directions, any axis in the x–y plane can be considered a principal axis of elasticity. As a result, the line of oscillation precesses undisrupted in the presence of rotation (figure 3(*a*)), allowing accurate measure of the angle of precession ϕ, given by [9]

$$\tan 2\phi = \frac{2\left(\omega_n^2 xy + \dot{x}\dot{y}\right)}{\omega_n^2(x^2 - y^2) + (\dot{x}^2 - \dot{y}^2)}. \tag{3}$$

In the case of a non-isotropic suspension where $k_{xx} \neq k_{yy}$ and $k_{xy} = k_{yx} \neq 0$, the location of the principal axes of elasticity is no longer arbitrary. These anisoelasticities disrupt the line of oscillation as it precesses away from the principal axes (figure 3(*b*)), which disrupts the measurements necessary to determine the precession angle [7]. Thus, an ideal suspension is one that is both isotropic and robust to environmental variations that could cause anisoelasticity, such as thermal fluctuations. These requirements motivate the choice of concentric rings as a suspension design.

3. Structural analysis

This section develops an analytical model to estimate the in-plane structural stiffness and confirm the isotropy of the proposed suspension. Finite element modeling is used to verify this result and to show the influence of thickness on the separation of desirable and undesirable resonant modes.

3.1. Analytical modeling

The model consists of a proof mass suspended above the substrate using a multiplicity of concentric rings (figure 4(*a*)) where the number of rings and the ring geometry are chosen to achieve a desired stiffness value. The rings are interconnected at 90° increments, with the outer ring being rigidly attached to an anchored frame. If the suspension is isotropic, the stiffness along both principal axes of elasticity must be the same (figure 4(*b*)). By calculating the deflection of the proof mass in response to a known arbitrary force **F** at an arbitrary angle α, an expression for the stiffness is found. In the analysis, we first solve for the deflection in the case of a single, fixed ring. Then the total deflection of the proof mass is calculated by summing the contributions of each subsequent ring using the reaction forces and moments from the previous ring as the applied forces and moments, assuming each ring interconnect is rigid. In a realistic implementation of the device, ring lengths will be at least two orders of magnitude larger than the maximum deflection. This validates the use of linear elasticity theory.

As the first step in the analysis of the overall model, we consider the deflection contribution of the inner ring. The inner ring is fixed at its connection points to the second ring and the rigid connection of the proof mass is modeled using constraint forces $(\lambda_1, \lambda_2, \lambda_3, \lambda_4)$ (figure 5(*a*)). If the interconnects are sufficiently rigid, the suspension has very high angular stiffness, preventing the proof mass from twisting. M_0 is the moment used to represent this angular deflection constraint. Due to symmetry, this model can be further decomposed to a quadrant of the ring (figure 5(*b*)) where the fixed end conditions at ends A and B are modeled using reaction forces and moments (R_x, R_y, M).

The corresponding reactions are calculated [10] as functions of the constraints and applied force and are used to find the total strain energy U of the curved member. If the radius r_1 is large compared to the thickness of the ring t, i.e. $r_1/t > 10$, the bending energy dominates the strain energy [10], and U can be expressed as

$$\begin{aligned} U &= \int_0^{\frac{\pi}{4}} \frac{\hat{M}_A^2}{2EI} r_1 \, \mathrm{d}\gamma + \int_0^{\frac{\pi}{4}} \frac{\hat{M}_B^2}{2EI} r_1 \, \mathrm{d}\theta \\ \hat{M}_A &= -r_1(1 - \cos\gamma) R_{x,A} - r_1 \sin\gamma \, R_{y,A} + M_A \\ \hat{M}_B &= r_1 \sin\theta \, R_{x,B} + r_1(1 - \cos\theta) R_{y,B} + M_B \end{aligned} \tag{4}$$

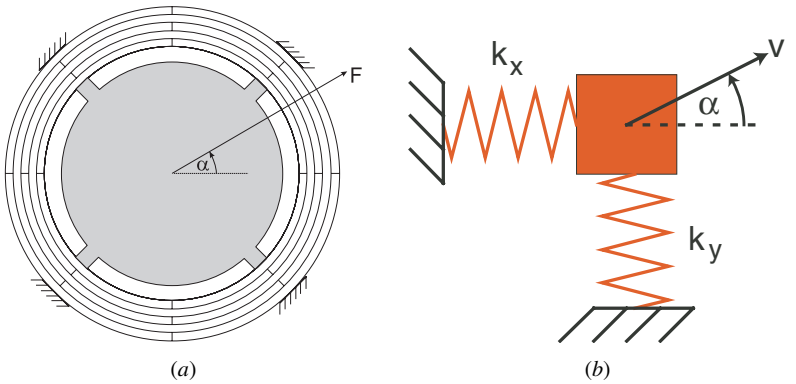

(*a*) (*b*)

Figure 4. (*a*) The gyroscope is modeled as a proof mass suspended by a multiplicity of concentric ring suspension members. The stiffness of the suspension is calculated by finding the deflection of the proof mass in response to a force **F** at an arbitrary angle α. (*b*) The stiffness in an arbitrary direction, **v**, can be decomposed into the contributions of the stiffnesses along the principal axes of elasticity, $2k_v = (k_x + k_y) + (k_x - k_y)\cos 2\alpha$. If the suspension is isotropic, $k_v = k_x = k_y$.

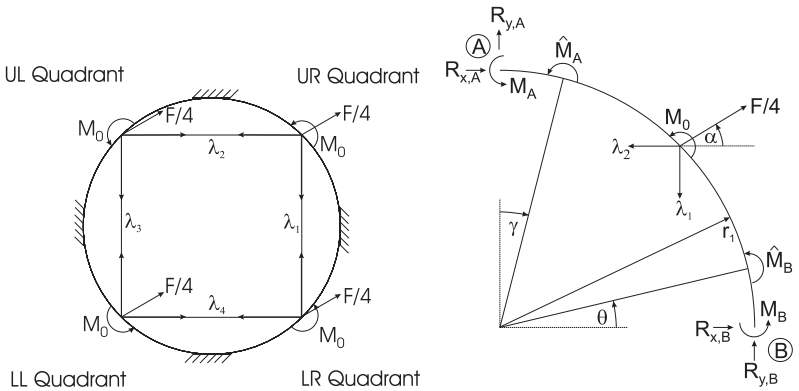

(*a*) (*b*)

Figure 5. (*a*) The inner ring contribution can be calculated from the contributions of each quadrant. The λ and M_0 represent constraint forces and constraint moments due to the rigid attachment of the proof mass. (*b*) The problem is further decomposed into the contributions of each quadrant. The deflection is found by differentiating the strain energy calculated from the reaction forces (R_x, R_y, M).

where $\hat{M}_A$ and $\hat{M}_B$ are the reaction induced moments at angles γ and θ from fixed ends A and B, respectively (see figure 5(*b*)). Here, the reaction forces and moments are functions of the applied force **F**, angle of applied force α, and the constraints [10]

$$R_{x,A} = -.2846F\cos\alpha - .1220F\sin\alpha + .4880\lambda_1 + 1.1382\lambda_2 + .7257(M_0/r_1)$$
$$R_{y,A} = .1220F\cos\alpha + .0346F\sin\alpha - .1384\lambda_1 - .4880\lambda_2 + .7257(M_0/r_1)$$
$$R_{x,B} = .0346F\cos\alpha + .1220F\sin\alpha - .4880\lambda_1 - .1385\lambda_2 - .7257(M_0/r_1)$$
$$R_{y,B} = -.1220F\cos\alpha - .2845F\sin\alpha + 1.1381\lambda_1 + .4880\lambda_2 - .7257(M_0/r_1)$$
$$M_A = .0160Fr_1\cos\alpha + .0018Fr_1\sin\alpha - .0073r_1\lambda_1 - .0641r_1\lambda_2 + .22577M_0$$
$$M_B = -.0019Fr_1\cos\alpha - .0160Fr_1\sin\alpha + .0641r_1\lambda_1 + .0076r_1\lambda_2 + .2257M_0$$

By Castiliano's theorem, the deflection of an elastic member in the direction of the applied force is equal to the change in strain energy with respect to the applied force [10],

$$\delta_{F,r_1} = \frac{\partial U}{\partial F} = \frac{r_1}{EI}\int_0^{\frac{\pi}{4}} \hat{M}_A\frac{\partial \hat{M}_A}{\partial F}\,\mathrm{d}\gamma + \frac{r_1}{EI}\int_0^{\frac{\pi}{4}} \hat{M}_B\frac{\partial \hat{M}_B}{\partial F}\,\mathrm{d}\theta. \tag{5}$$

A similar solution is arrived at for each of the four quadrants, leading to a total of eight unknowns consisting of four λ constraints and four M_0 constraints. By assuming zero deformation in the constraints, the unknowns are eliminated by symmetry constraints

$$\delta_{\lambda_1,\mathrm{UR}} + \delta_{\lambda_1,\mathrm{LR}} = \delta_{\lambda_2,\mathrm{UR}} + \delta_{\lambda_2,\mathrm{UL}} = 0$$
$$\delta_{\lambda_3,\mathrm{UL}} + \delta_{\lambda_3,\mathrm{LL}} = \delta_{\lambda_4,\mathrm{LL}} + \delta_{\lambda_4,\mathrm{LR}} = 0$$
$$\delta_{M_0,\mathrm{UR}} = \delta_{M_0,\mathrm{LR}} = \delta_{M_0,\mathrm{LL}} = \delta_{M_0,\mathrm{UL}} = 0.$$

Here UR, LR, LL and UL designate the upper right, lower right, lower left and upper left quadrants of the inner ring, respectively (see figure 5(*a*)). Solving the system of equations simultaneously yields

$$\delta_{F,r_1} = \frac{r_1^3}{4EI}(4.017\times 10^{-4}F). \tag{6}$$

The final step in the analysis is to add the contributions of each of the subsequent rings using a similar analysis procedure as

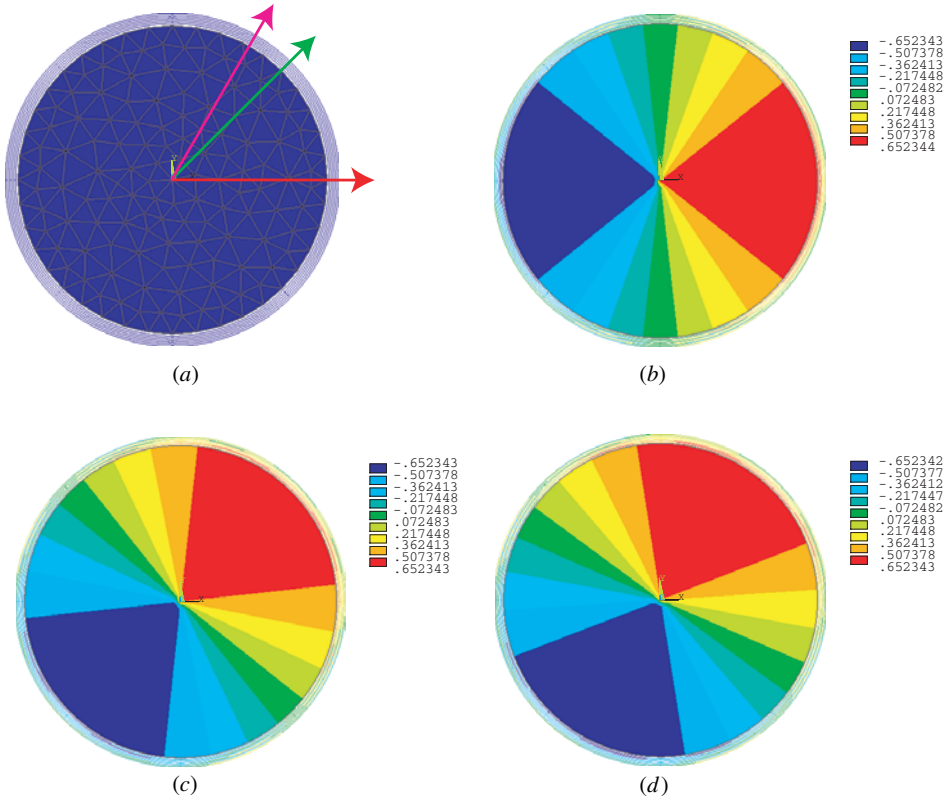

Figure 6. The uniformity of the suspension was confirmed by modeling the system using the FEM package ANSYS. The suspension was modeled using three dimensional beam elements, while the proof mass was modeled using three dimensional shell elements. The proof mass was subjected to the same load in the directions of (*a*) 0, 45 and 60°. The corresponding radial displacements as shown in (*b*), (*c*) and (*d*), respectively, were equal, which confirms the isotropy of the suspension.

for the first ring. We find the contribution of the second ring by modeling it as rigidly attached where it would be connected to the third ring. The reaction forces of the inner ring are used as the applied forces on the second ring. Using the same solution procedure as for the inner ring, with the simplification that the second ring is unconstrained ($\lambda = M_0 = 0$), the deflection of the top and bottom quadrants of the second ring is

$$\delta_{F,r_2} = \frac{F}{EI}\left(0.0002r_2^3\cos^2\alpha - 0.0001r_2^2 r_1\cos^2\alpha + 0.0001r_2^3\sin^2\alpha\right). \quad (7)$$

Letting the spacing between the rings be given as $\Delta r = r_2 - r_1$, equation (7) can be written as

$$\delta_{F,r_2} = \frac{r_2^2}{4EI}(r_2 + \Delta r\cos^2\alpha)(4.0104\times10^{-4}F). \quad (8)$$

If the spacing is sufficiently small compared to the radius ($\Delta r/r_2 \ll 1$), then (8) simplifies to

$$\delta_{F,r_2} = \frac{r_2^3}{4EI}(4.0104\times10^{-4}F). \quad (9)$$

With this assumption, the same result is found for the left and right quadrants. Assuming that the bending moment of inertia (I) and the modulus of elasticity (E) are identical for all rings, we see that this deflection varies only with radius when compared to the deflection of the inner ring, equation (6). By induction, this expression for the ring deflection will propagate to each subsequent ring. The generalized stiffness can be written as force divided by deflection,

$$k_r(r) = 9957.68\frac{EI}{r^3}. \quad (10)$$

The total stiffness of the system can be found by summing the stiffness of all the rings in series

$$k_{\text{tot}} = \frac{9957.68EI}{\sum_{i=1}^{n} r_i^3} \quad (11)$$

where n is the number of rings. The final solution is not a function of α, so it is concluded that this stiffness is independent of the angle of the applied force, thus verifying the isotropy of the suspension.

3.2. Finite element modeling

To verify the analytical model, a finite element model was constructed using the ANSYS multiphysics FEA package. Since the length to width ratio of the rings is large, the suspension was modeled using massless BEAM4, three dimensional beam elements. The proof mass was modeled using three dimensional shell elements, SHELL93, with a thickness of 2 μm (a typical structural thickness for surface micromachining technologies). Using a geometry for a practical design of the gyroscope, a six ring suspension is used where the radii of the rings are 303.5, 306.5, 309.5, 312.5, 315.5 and 318.5 μm and the width of each ring was 1 μm. The Young's modulus was assumed to be 169 GPa for this analysis. A known force of 1 μN was applied at the center of the proof mass in three varying in-plane directions (0, 45 and 60°). The in-plane radial deflections of the proof mass were found to be the same in all three cases (figure 6). Due to the symmetry of the structure, this demonstrates that

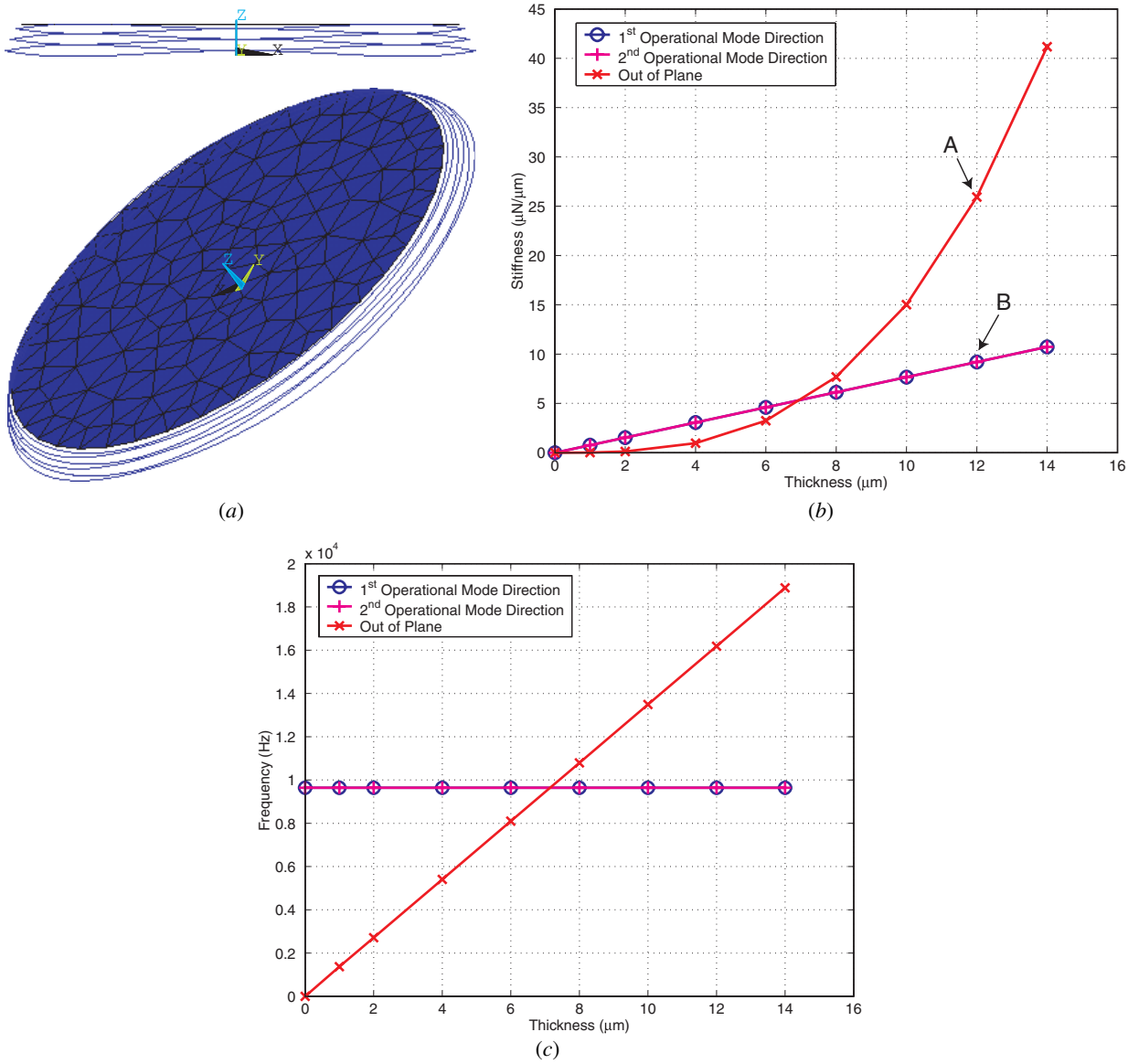

Figure 7. (*a*) The use of thin structural layers in the design of the suspension results in undesirable out-of-plane modes. (*b*) The parametric analysis of the suspension reveals that the out-of-plane stiffness increases as thickness cubed, while the in-plane stiffness is linear. At 12 μm thickness, the out-of-plane stiffness (point A) is nearly three times larger than the in-plane stiffness (point B). (*c*) Since mass also increases linearly, the in-plane natural frequency remains constant while the out-of-plane natural frequency increases linearly.

the suspension is uniformly stiff in all radial directions. The stiffness, calculated as force divided by deflection, results in a value of 1.48 N m^{-1}. From the previous section, since the spacing of the rings in the simulation is sufficiently smaller than the radii ($\Delta r/r \ll 1$), equation (11) can be used to find the stiffness analytically. Using the same geometries as the FEA simulation, the analytical expression gives a stiffness of 1.53 N m^{-1}, yielding a close match to the FEA acquired results, with a difference of only 4.5%. While some level of anistropy is to be expected as seen in equation (8), this effect was observed to be orders of magnitude smaller than the actual calculated stiffness values.

3.3. Mode separation

For the operation of the gyroscope, it is desirable to design the device where the operational modes are separated from any undesirable modes. Surface micromachining has limitations on the thickness of structural layers and these restrictions yield a low out-of-plane stiffness, resulting in undesirable out-of-plane modes (figure 7(*a*)). It is possible to compensate for this effect by utilizing thicker structural layers.

A modal analysis based on the same FEA model as in the previous section is used to identify the effect of varying thickness on the performance of the device. Since the length of the rings is large compared to the thicknesses used in this study, the choice of beam elements is still appropriate. As thickness (t) increases, the in-plane bending moment of inertia, and therefore the in-plane stiffness of the rings, increases linearly ($k_r = f(t)$) (figure 7(*b*)). In comparison, the out-of-plane moment of inertia, and thus the out-of-plane stiffness, increases as thickness cubed ($k_z = f(t^3)$). Since the mass also increases linearly with thickness, the in-plane natural frequencies remain constant ($\omega_{n,r} = \sqrt{k_r/m} = \text{const}$),

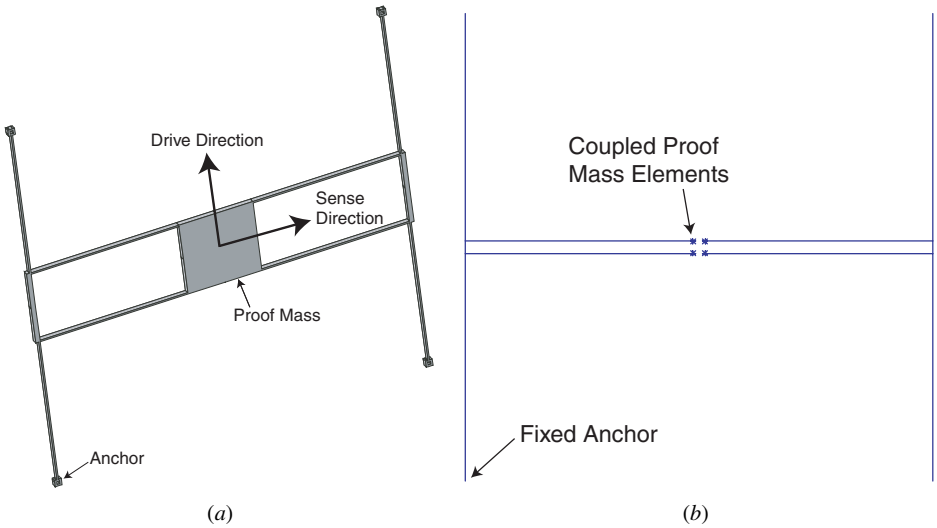

Figure 8. (*a*) A comparative thermal analysis is done with a device utilizing an H-type suspension. The operational mode resonance frequencies are identical to those of the ring suspension system through appropriate choices in geometry. (*b*) The finite element model of the system is made using three dimensional beam and mass elements for the suspension and proof mass, respectively. The model is subjected to thermal loading and the prestressed resonant modes are found.

while the out-of-plane natural frequencies increase linearly ($\omega_{n,z} = \sqrt{k_z/m} = f(t)$) (figure 7(*c*)). From the simulation, at an optimal thickness of 12 μm, the out-of-plane stiffness is almost three times greater than the in-plane stiffness, thus providing an appropriate mode separation between desirable and undesirable modes of operation of the gyroscope.

4. Sensitivity analysis

In MEMS gyroscopes, it is necessary to maintain matching between the drive and sense modes in order to maximize sensitivity. Even deviations as low as 1% between drive and sense mode frequencies result in errors as high as 20% in the output signal gain [11]. An important design consideration is to choose a suspension that is robust to environmental effects, such as temperature changes, that can cause modal mismatch. In this section we compare the effects of thermal fluctuations on the ring suspension with those on an H-type suspension (figure 8) commonly used in MEMS gyroscope designs [8].

4.1. Effect of temperature changes

The effects of temperature changes on the frequency of a system can be decoupled into three different effects: changes in the modulus of elasticity, thermal expansion and thermally induced stresses. The influence of the modulus of elasticity and thermal expansion on the resonant frequency ω_r of the system, in general, can be approximated as

$$\omega_r(T_f) = \omega_r(T_0) + \omega_r(T_0) TC_f \Delta T \tag{12}$$

where ΔT is the change in temperature and T_0 and T_f are the initial and final temperatures, respectively. TC_f is the temperature coefficient for the resonant frequency, which can be expressed by [12]

$$TC_f = \tfrac{1}{2}(TC_E - TC_h) \tag{13}$$

where TC_E is the temperature coefficient of Young's modulus for fine-grained polysilicon given as [13] -75 ppm $^\circ\mathrm{C}^{-1}$ and TC_h is the coefficient of thermal expansion, 2.0 ppm $^\circ\mathrm{C}^{-1}$.

Without some mechanism of stress relief, thermally induced stresses become the dominating factor in frequency mismatch. In the case of the H-type suspension, the beams across the suspension can be assumed to be stress free while those fixed to the substrate are susceptible to stresses. Under tensile stress, the drive and sense frequencies are given by [8]

$$\omega_{\text{drive}} = 2\sqrt{\frac{Ez_0}{m}\left(\frac{w}{L}\right)^3} \tag{14}$$

$$\omega_{\text{sense}} = 2\sqrt{\frac{Ez_0}{m}\frac{\kappa^2}{12}\frac{w}{L}\left(1 - \frac{2}{\kappa}\frac{w}{L}\frac{\cosh\left(\kappa\frac{L}{w}\right) - 1}{\sinh\left(\kappa\frac{L}{w}\right)}\right)^{-1}} \tag{15}$$

where $\kappa = \sqrt{12\epsilon_x}$ and ϵ_x is the axial strain. Assuming that due to rigid attachment to the truss, the length of the anchored beam is not free to expand, the strain can be approximated as $\epsilon_x = TC_h \Delta T$. Using the same solution methodology [8], the sense frequency under compressive stress is

$$\omega_{\text{sense}} = 2\sqrt{\frac{Ez_0}{m}\frac{\kappa^2}{12}\frac{w}{L}\left(-1 - \frac{2}{\kappa}\frac{w}{L}\frac{\cos\left(\kappa\frac{L}{w}\right) - 1}{\sin\left(\kappa\frac{L}{w}\right)}\right)^{-1}}. \tag{16}$$

To capture all these effects, finite element modeling using ANSYS was done to compare the H-type suspension with the ring suspension. Each suspension was modeled using BEAM4 elements with a thickness of 2 μm and a width of 1 μm. The radii for the ring suspension are identical to those in the previous model, while an appropriate choice of 95.55 μm for the beam lengths in the H-type suspension was made to match the same operational mode frequencies as in the ring suspension. Each proof mass was modeled using MASS21, three dimensional mass elements. The four proof mass elements were then coupled using constraint equations.

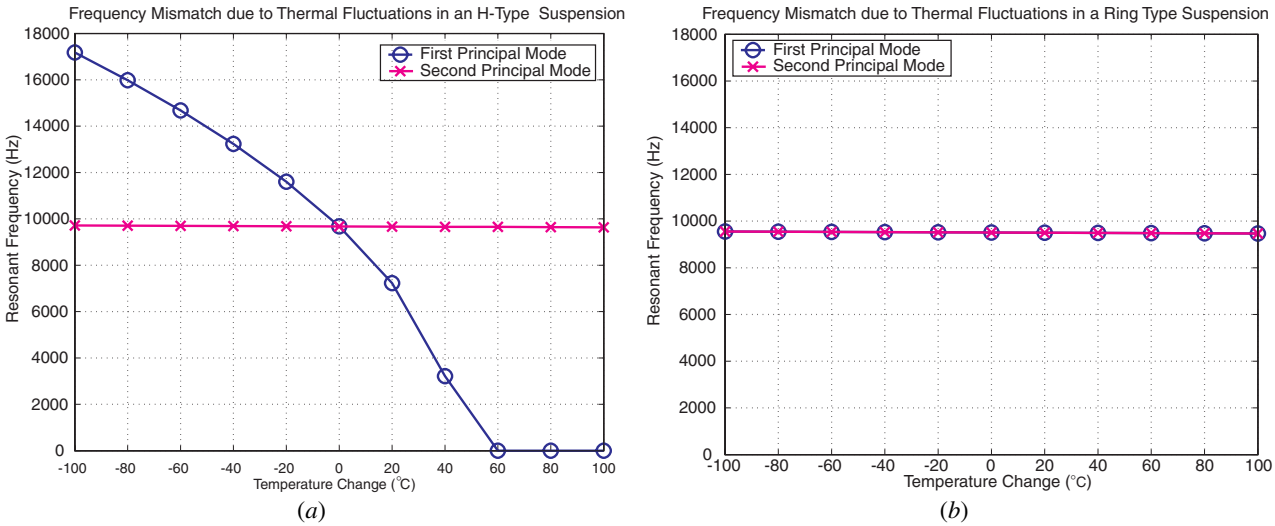

Figure 9. (*a*) Without a form of stress relief, thermal fluctuations cause large frequency mismatches in the H-type suspension, with buckling occurring at higher positive temperatures. (*b*) In contrast, the ring suspension allows for stress relief and as a result, the modes of the ring suspension remain matched during varying temperature changes.

Each system was modeled assuming an effective mass of 4.18×10^{-10} kg. The models were subjected to global heating temperatures between -100 and 100 °C and a static analysis was run with prestress effects turned on. The prestress effects stored the stresses from the static analysis, which were then applied to a modal analysis. Prior to the modal analysis, the nodal coordinates were updated with the deflections from the static analysis and Young's modulus was changed to reflect its inherent temperature dependence

$$E(T_f) = E(T_0) + E(T_0)TC_E\Delta T \tag{17}$$

where the initial value for Young's modulus $E(T_0)$ was 169 GPa.

From the analysis of the H-type suspension (figure 9(*a*)), the drive mode shows slight deviations from its original frequency of 9676 Hz mostly due to changes in Young's modulus. The sense direction shows a low resilience to stress and exhibits a frequency change of 7639 Hz from its original value of 9674 Hz under negative temperature changes (tensile stress), yielding a frequency mismatch of 79% between drive and sense. In addition, under high positive temperature changes (compressive stress), the suspension buckles due to high stresses, resulting in failure of the device. In contrast, the ring suspension allows for stress relief and disperses stresses uniformly due to axial symmetry. As a result, the modes of the ring suspension remain matched to their original values of 9612 and 9617 Hz in the presence of the same thermal loading as in the case of the H-type suspension (figure 9(*b*)). Isotropic changes in the frequency are a result of uniform expansion of the suspension and changes in Young's modulus and result in a maximum uniform frequency change of 0.4% in the temperature range for both suspension types.

4.2. Residual stress

Residual stress is a common by-product in many MEMS fabrication processes, resulting in degraded performance of micromachined devices. As an example, we consider the case of the studied gyroscope being fabricated using the Cronos MUMPS process [14] where heated polysilicon is deposited on a sacrificial oxide layer. Since the polysilicon is rigidly attached to the sacrificial layer, one mechanism of residual stress is thermal stress that develops as the polysilicon cools to room temperature due to thermal mismatch between the polysilicon and the oxide. After subsequent release of the oxide layer, a certain amount of stress remains, which varies from run to run. The gyroscope utilizes the POLY1 structural layer, where the residual stress for the MUMPS-42 run, for example, is given as 9 MPa in compression. Since thermal stress can be calculated by $\sigma = ETC_h\Delta T$, the effect of residual stress can be modeled by thermally loading the device to a temperature of 23.67 °C. From the previous section, we see that operational modes of the ring suspension remain matched under such temperature loading. In contrast, if an H-type suspension were to be implemented using the same technology and suspension geometry, the residual stress would result in a frequency mismatch of 31%.

5. Conclusion

In this paper, we have structurally characterized a MEMS angular gyroscope by evaluating the stiffness of the novel ring suspension system and determining the resonant modes of operation and corresponding resonant frequencies. It has been demonstrated that the six concentric and interconnected ring suspension provides the necessary isotropy required for the operation of the device. Further, we have developed a close form solution for the stiffness of the suspension, which is applicable to any suspension of this type, given any arbitrary number of rings, and confirmed this result using finite element modeling. It has also been shown that using a fabrication technology utilizing thick structural layers shifts the undesirable modes of operation to a higher frequency range, thus increasing the immunity of the device to undesirable excitations. A thermal comparison between the existing device and a device utilizing an H-type spring suspension shows that the ring suspension is

significantly more resilient to temperature changes as well as residual stress effects that develop during fabrication of the device.

Acknowledgment

The authors would like to thank the Department of Defense which is partially sponsoring this work through a 2001 National Defense Science and Engineering Graduate Fellowship.

References

[1] Yazdi N, Ayazi F and Najafi K 1998 Micromachined inertial sensors (invited paper) *Proc. IEEE* **86** 1640–59
[2] Foucault J B L 1851 Dèmonstration Physique au Mouvement de Rotation de la Terre au Moyen du Pendule *C. R. Acad. Sci.* **32** 135–8
[3] Putty M and Najafi K 1994 A micromachined vibrating ring gyroscope *IEEE Solid State Sens. and Act. Work. (Hilton Head Island, SC)* (Cleveland Heights, OH: Transducer Res. Found) pp 213–20
[4] Hopkin I 1997 Performance and design of a silicon micromachined gyro *Proc. Symp. Gyro Tech. (Stuttgart, Germany)* pp 1.0–1.10
[5] Shkel A and Howe R T 2002 Micro-machined angle-measuring gyroscope US Patent 6481285
[6] Shkel A, Horowitz R, Seshia A and Howe R T 1999 Dynamics and control of micromachined gyroscopes *The Amer. Cont. Conf. (San Diego, CA)* vol 3 (Piscataway, NJ: IEEE) pp 2119–24
[7] Shkel A, Howe R T and Horowitz R 1999 Modeling and simulation of micromachined gyroscopes in the presence of imperfections *1999 Int. Conf. on Mod. and Sim. of Micro. (San Juan, Puerto Rico)* (Cambridge, MA: Computational Publications) pp 605–8
[8] Clark W A 1997 Micromachined vibratory rate gyroscopes *PhD Thesis* UC Berkeley
[9] Friedland B and Hutton M 1978 Theory and error analysis of vibrating-member gyroscope *IEEE Tran. Auto. Cont.* **AC-23** 545–56
[10] Young W C 1989 *Roark's Formulas for Stress and Strain* vol 6 (New York: McGraw-Hill)
[11] Netzer E and Porat I 1995 A novel vibratory device for angular rate measurement *J. Dyn. Sys., Meas. Cont.* **117** 585–91
[12] Remtema T and Lin L 2000 Active frequency tuning for microresonators by localized thermal stressing effects *Solid-State Sens. and Act. Work. (Hilton Head Island, SC)* (Cleveland, OH: Transducers Res. Found) pp 363–6
[13] Lin L, Howe R T and Pisano A P 1998 Microelectromechanical filters for signal processing *J. Micro. Sys.* **7** 286–94
[14] http://www.memsrus.com